
This manuscript has been submitted for publication in EARTH AND SPACE SCIENCE. Please note that this article has not been peer-reviewed and is currently undergoing peer review for the first time. Subsequent versions of this manuscript may have slightly different content. If accepted, the final version of this manuscript will be available via the 'Peer-reviewed Publication DOI' link on the right-hand side of this webpage. Please feel free to contact any of the authors; we welcome feedback

Evaluation of Vegetation Bias in InSAR Time Series for Agricultural Areas within the San Joaquin Valley, CA

Kelly Devlin¹ and Rowena B. Lohman¹

¹Department of Earth and Atmospheric Sciences, Cornell University, Ithaca, NY.

Corresponding author: Kelly Devlin (krd86@cornell.edu)

Three key points of research

- We quantify the contribution of bias from vegetation and soil moisture effects on InSAR phase and time series
- We find biases of ~2-4 cm/yr within agricultural fields, with the largest biases occurring in cotton fields within Tulare Lake basin
- We suggest removing agricultural fields from time series analysis can help mitigate phase biases

Plain Language Summary

We examine maps of ground displacement over the San Joaquin Valley, CA, which contains a variety of crop types. We use information about ground cover and crop type to isolate the average effects of individual agricultural fields. We find that some fields can lead to an overestimation of subsidence by about 2-4 cm/yr. It is important to understand the effect of agricultural activity on displacement maps in order to accurately interpret where and how fast subsidence is occurring. Even something as simple as removing the agricultural fields from the data at an early stage, before interpretation, can remove these false signals.

Abstract

Agricultural regions present a particularly difficult set of challenges during interferometric synthetic aperture radar (InSAR) displacement time series analyses due to the existence of abrupt transitions in land use over short spatial scales and rapid temporal changes associated with different stages of the agricultural cycle. Plant growth and soil moisture changes can introduce phase biases within interferograms that could be misinterpreted as displacement. We analyze a full-resolution, multi-year SAR time series over California's San Joaquin Valley, an intensively cultivated region producing a wide variety of crops. Using independent information about land cover and crop type, we isolate the effects of individual crops on backscatter amplitude, interferometric phase change, and interferometric coherence over space and time. We determine the temporal behavior of the phase changes associated with several key crop types by isolating the difference between the phase of pixels averaged over each agricultural field and the phase values of pixels in nearby roads, fallow, and developed areas. We find that some fields are associated with a bias of ~2-4 cm/yr of apparent subsidence, with strong seasonal variability in the degree of bias. When InSAR imagery is spatially averaged or filtered, these biases also impact the inferred phase in nearby roads and other land cover types. We show that even a simple approach, where pixels associated with agricultural fields are removed or masked out before further processing, can mitigate the crop-related biases that we observe in the study area.

1. Background

Many intensively cultivated agricultural regions around the world are heavily reliant on groundwater extraction. Groundwater overdraft is a widely recognized problem globally, with numerous large aquifers being depleted faster than they can recharge (e.g., Gleeson et al., 2012; Richey et al., 2015; Wada et al., 2010). The adverse effects of groundwater overdraft include saltwater intrusion, damage to ecosystems, land subsidence, and permanent aquifer storage loss (e.g., Asner et al., 2016; Hasan et al., 2023; Nishikawa et al., 2009; Rohde et al., 2024).

One place where the effects of groundwater extraction have been particularly well-documented is in the San Joaquin Valley, California. The San Joaquin Valley produces over half of

California's agricultural output, employs about 340,000 people, and generates over \$24 billion each year in revenue (Escriva-Bou et al., 2023). Continued, market-driven expansion of crops, particularly perennial orchards, is increasing the likelihood of frequent water shortages in the future (Mall and Herman, 2019). Groundwater is increasingly relied on during times of drought, which further exacerbates the unsustainability of current water management practices and policy (Escriva-Bou et al., 2020; Petersen-Perlman et al., 2022). Future efforts to improve water management practices and policies will require reliable estimates of the amount and distribution of groundwater withdrawal (Butler et al., 2020). Accurate maps of land subsidence are one type of observation that can contribute to our understanding of the groundwater budget for this and other aquifers around the world.

Land subsidence in the San Joaquin Valley due to groundwater overdraft has been recorded for decades, with the first geodetic observations in the 1920s (Poland et al., 1975). Since the 1990s, interferometric synthetic aperture radar (InSAR) has been used to study ground displacements due to a range of subsurface processes (e.g., Massonnet et al., 1993), including subsidence associated with the extraction of groundwater (e.g., Amelung et al., 1999; Chaussard et al., 2014; Gao et al., 2018; Hussain et al., 2022; Motagh et al., 2017). Numerous studies document subsidence in the San Joaquin Valley using InSAR, GPS, and ground truth measurement (e.g., Farr, 2016; Kang and Knight, 2023; Murray and Lohman, 2018; Neely et al., 2020). Inferred subsidence rates were as high as 30 cm/yr during the 2012-2016 California drought. However, InSAR observations are also impacted by vegetation and soil moisture, factors that are not accounted for in most InSAR analyses (e.g., Dall, 2007; De Zan and Gomba, 2018; Gabriel et al., 1989; Zheng et al., 2022; Zwieback et al., 2015).

In this study, we evaluate potential biases due to contributions from cropland over the southern San Joaquin Valley (Figure 1). We compare the InSAR phase averaged over individual fields with the phase of nearby roads and stable surfaces. This approach allows us to separate the effect of crop growth, irrigation and other agricultural activities that vary on the spatial scale of individual fields from the much larger spatial scale features associated with aquifer-related subsidence and tropospheric variability. In Section 2, we describe the datasets used in our analysis. In Section 3, we briefly discuss geophysical factors that affect InSAR phase and describe our method for calculating the phase bias associated with individual fields as well as the resulting displacement time series and inferred velocity map. In Section 4, we report the results of our methodology, including the behavior of specific crops over time and the results of our two different types of velocity inversions. Finally, in Section 5, we discuss the fields and crops that have the largest biases. We comment on the potential overestimation of subsidence in InSAR time series and provide recommendations on the appropriate strategy for dealing with these biases.

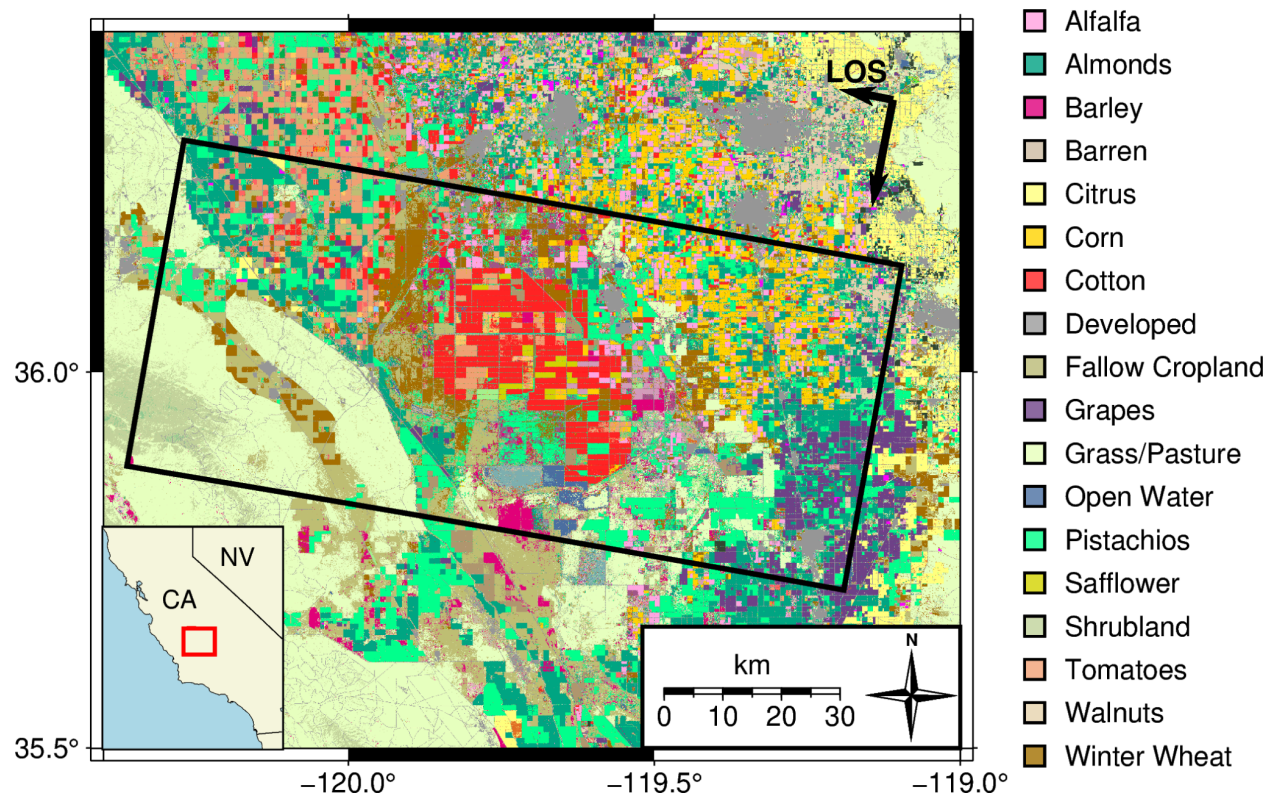


Figure 1: Location of study site within San Joaquin Valley, CA (inset, panel location indicated with red rectangle). Colors indicate crop and ground cover type in 2020 based on USDA Cropland Data Layer database (USDA NASS, 2021). Black box outlines extent of SAR footprint (subset of Sentinel-1a/b Descending Track 144). We use 129 SAR acquisitions from 08/2019 - 09/2021 with 6 day repeats.

2. Data

We use freely available C-band SAR imagery from descending Track 144 of the European Space Agency's Sentinel-1a/b mission acquired between 2019/08/14 and 2021/09/20 on a 6-day repeat interval (129 acquisitions). We use crop information between 2019 and 2021 from the Cropland Data Layer (CDL) created by the United States Department of Agriculture (USDA), National Agricultural Statistics Service, Research and Development Division, Geospatial Information Branch, Spatial Analysis Research Section (USDA NASS, 2021). The CDL is a freely available geospatial dataset of Land Cover Land Use Change (LCLUC) and crop classification offered at annual intervals at 30-m pixel resolution derived from remotely-sensed data. The current CDL Program uses the Landsat 8 and 9 OLI/TIRS sensor, the Disaster Monitoring Constellation (DMC) DEIMOS-1 and UK2, the ISRO ResourceSat-2 LISS-3, and the ESA SENTINEL-2 A and B sensors (USDA NASS, 2021).

We use Google Earth Engine (Gorelick et al., 2017) to obtain Landsat 8 Surface Reflectance imagery courtesy of the U.S. Geological Survey and Sentinel-2 MSI: MultiSpectral Instrument, Level-2A imagery (Copernicus Sentinel-2 (processed by ESA), 2021) acquired between

2019/08/15 and 2021/09/23 (205 acquisitions). Landsat 8 and Sentinel-2 imagery are available at 30-m and 10-m pixel resolutions, respectively. We use these Landsat 8 and Sentinel-2 optical imagery to calculate normalized difference vegetation index (NDVI) within each field. NDVI is defined as:

$$NDVI = \frac{NIR - RED}{NIR + RED} \quad (1)$$

where NIR is the observed reflectance of the near-infrared band and RED is the observed reflectance of the red band. NDVI values are, by definition, bounded within the range $[-1,1]$, with higher values generally indicating healthier or denser vegetation.

3. Methods

In this section, we review standard terminology used in interferogram analysis, then describe our InSAR processing workflow, from individual interferograms through time series analysis (Figure 2). The phase of a full resolution, unfiltered interferogram can be expressed (modulo 2π) as:

$$\varphi_{ifg} = \varphi_{disp} + \varphi_{atm} + \varphi_{topo} + \varphi_{srf} + \varphi_{other} \quad (2)$$

where φ_{ifg} is the phase of the interferogram, φ_{disp} is the ground displacement vector projected onto the satellite's line-of-sight (LOS), φ_{atm} is the atmospheric delay, φ_{topo} is from digital elevation model (DEM) errors, φ_{srf} is the contribution from surface properties, such as soil moisture, vegetation and their temporal changes, and φ_{other} includes all other noise sources such as thermal and decorrelation noise (Zebker and Villasenor, 1992).

For this study, we focus on isolating φ_{srf} from the other factors and evaluating phase contributions associated with a given crop type. To isolate φ_{srf} , we rely on the assumption that φ_{disp} and φ_{atm} have spatial scales that are large relative to the size of individual agricultural fields, and also assume that φ_{other} is random in time with mean zero and will introduce a negligible contribution to our final time series. Because the San Joaquin Valley has very low topographic relief, we also neglect consideration of φ_{topo} in this work. We isolate φ_{srf} at any location in a given interferogram by taking the difference in phase between an agricultural field and any adjacent roads and other stable surfaces (Section 3.2), under the assumption that stable surfaces and fallow fields will have less sensitivity to soil and vegetation moisture changes than the agricultural fields.

To assess and control for data quality, we use several metrics. The first is the interferometric complex coherence, γ , defined as:

$$\gamma = \frac{\langle ab^* \rangle}{\sqrt{\langle aa^* \rangle \langle bb^* \rangle}} \quad (3)$$

where a is the first SAR acquisition, b is the second SAR acquisition, $*$ denotes the complex conjugate, and $\langle \bullet \rangle$ denotes a spatial average. We use the complex coherence magnitude, $|\gamma|$, (simply referred to “coherence”, below) which falls in the range $[0, 1]$. Low values of coherence (decorrelation) are associated with more phase variability within the spatial averaging window, and high values of coherence indicate data that is more uniform over that scale. In the San Joaquin Valley, we expect decorrelation when there are rapid changes in vegetation and soil moisture properties between two SAR acquisitions, such as during times of tilling, irrigation, crop growth, and harvesting. During these time periods, the phase values have little physical meaning and appear as uniform random noise within any fields associated with these activities.

Another metric of data quality we used is the phase stability, χ , similar to (Hooper et al., 2004), which is defined as:

$$\chi = \frac{1}{n-1} \left| \sum_{i=1}^{n-1} \exp \left\{ j \left(\varphi_{i,i+1} - \langle \varphi_{i,i+1} \rangle \right) \right\} \right| \quad (4)$$

where n is the number of SAR acquisitions, $\varphi_{i,i+1}$ and $\langle \varphi_{i,i+1} \rangle$ are the unfiltered and filtered phase for interferogram between dates i and $i+1$, respectively. $\langle \varphi_{i,i+1} \rangle$ is calculated by taking the spatial average of the phase; we perform our calculation over a 4 azimuth x 20 range window. Similar to coherence above, phase stability falls in the range $[0, 1]$. Low phase stability values indicate that a pixel’s behavior is temporally inconsistent to its neighbors within the spatial averaging window. Conversely, high phase stability values indicate that a pixel’s behavior is temporally consistent with its neighbors.

3.1 SAR imagery preparation

We generate a full-resolution coregistered series of single look complex (SLC) imagery using the open-source InSAR Scientific Computing Environment version 2 (ISCE2) (Rosen et al., 2012) and the Sentinel stack processor (Fattahi et al., 2017). We remove topographic effects using the Shuttle Radar Topography Mission (SRTM) DEM (Farr et al., 2007). We use our coregistered SLC stack to generate 128 sequential six day full-resolution interferograms. We normalize the amplitude of each interferogram to reduce the dependence of the phase on . We apply several thresholds to mask out unreliable pixels. We mask out pixels with coherence ≤ 0.3 in each interferogram. We mask out all pixels with median amplitude ≤ 34 dB over all dates. This removes pixels within the Tule River, which is immediately adjacent to several of the roads in our study site. Additionally, we mask out all pixels with phase stability ≤ 0.4 to only include pixels that behave similarly to their neighbors when averaged over the entire study period. For our analysis below, we resample CDL products and NDVI products onto the range-doppler coordinate system of the original, full-resolution SLC imagery. When we directly compare NDVI to InSAR observations, we interpolate the NDVI time series onto the dates of the SAR imagery.

3.2 Field-specific analysis

Our goal is to compare the average interferometric phase of each individual field with the average interferometric phase of nearby roads and other stable surfaces. To identify individual fields, we select all pixels labeled in the CDL as one of six crops (almonds, cotton, grapes, pistachios, tomatoes, and winter wheat) any year between 2019 and 2021. We perform a series of morphological operations based on bitmaps of the distribution of each crop. Specifically, we use a 10 azimuth x 5 range kernel to erode over seven iterations and dilate over six iterations. This process reduces the number of isolated pixels within and around each field. We then identify the connected components based on the resulting bitmap associated with each crop. We assign each individual field an identification number. This process identifies 3167 agricultural fields that cover 26% of the total area of our study site (Figure S1a). To identify roads and other stable surfaces, we select all pixels labeled in the CDL as developed or barren at any point between 2019 and 2021. We also include any pixel always labeled fallow between 2019 and 2021. These criteria capture many dirt roads within our study site as well as other stable pixels outside the agricultural fields. These pixels cover 11% of the total area of our study site (Figure S1b).

We track several metrics for each field within each interferogram: SLC backscatter amplitude, average phase bias per field (φ_{bias}), and coherence (γ). We define average phase bias as the difference between the average phase within a single field (φ_{field}) and the average phase of the surrounding stable pixels (φ_{dev}) (Figure 2):

$$\varphi_{bias} = \text{arg}(\overline{\varphi}_{field} \overline{\varphi}_{dev}^*) \quad (5)$$

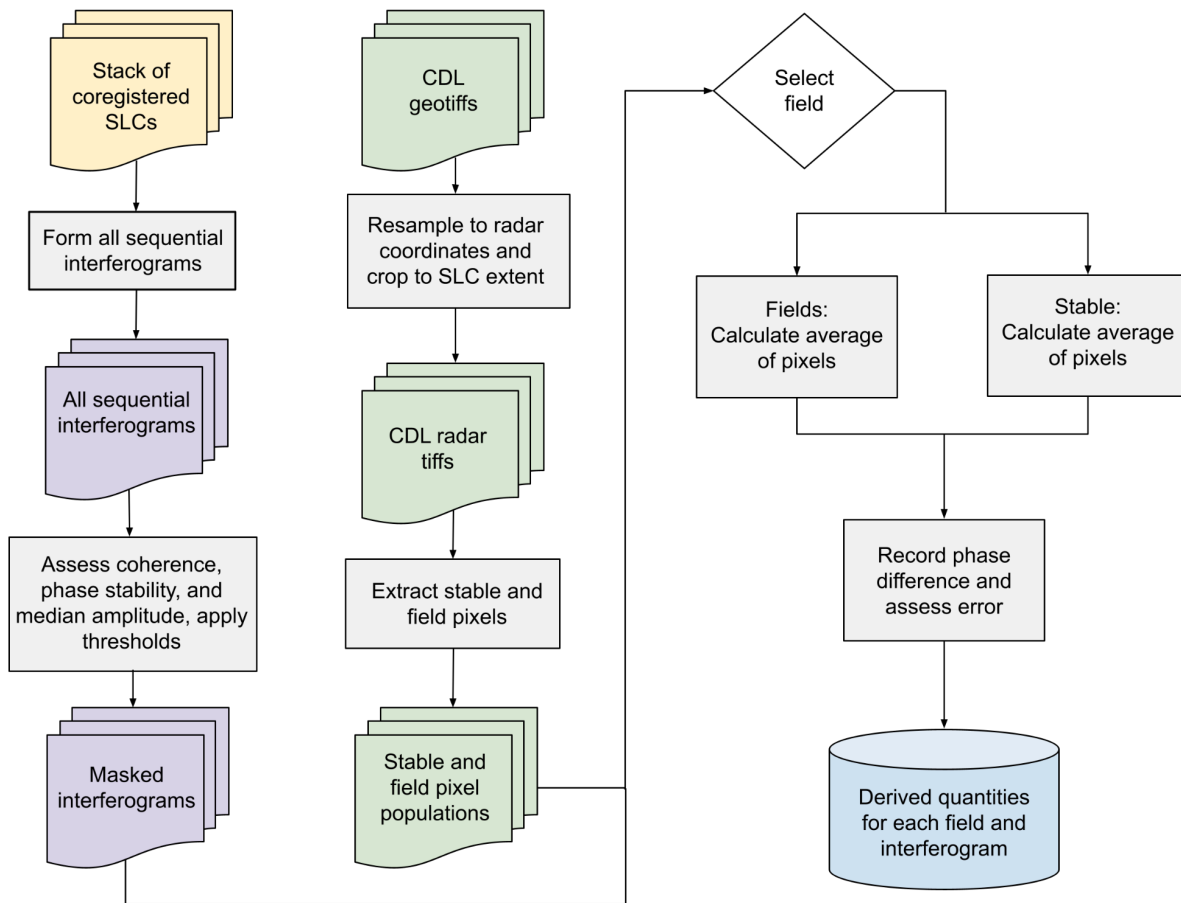


Figure 2: Workflow from raw data to interferograms for individual fields. Initial and end result datasets represented by bolded outline. Colors indicate CDL and CDL-derived products (green), coregistered SLCs (yellow), complex-valued products from InSAR (purple), and the final dataset with derived quantities for each field and interferogram (blue). Gray rectangles represent manipulation of datasets and white diamond represents selection of chosen crop for masking. Parallel lines indicate identical steps taken on both interferogram stacks independently.

3.3 Time series analyses

To quantify the contribution of phase biases within agricultural fields on displacement time series, we perform two types of time series analysis - one where we compare the results of using masked vs. masked versions of the real interferograms, and one where generate synthetic interferograms based on the phase estimates for each field and time interval as described in Section 3.2.

3.3.1 Masked vs. unmasked real-data time series

As described above, the study area is marked by very heterogeneous land cover, with sparse networks of roads, few cities, and natural terrain, interspersed between large agricultural fields. The roads are narrow relative to the filtering and spatial averaging scales that are typically used in InSAR processing, so their interferometric phase will tend to be “corrupted” by the phase in the adjacent fields during most InSAR processing workflows. To assess the potential impact of filtering/averaging over a mix of stable and agricultural pixels, we perform two time series analyses - one with the original set of interferograms and one where we mask out all but the stable pixels (as described in Section 3.2) at the highest resolution before any further processing.

We use the spatial resolutions and filtering choices used in the JPL-Caltech Advanced Rapid Imaging and Analysis (ARIA) project (Bekaert et al., 2019), which provides a free and open archive of Sentinel-1 unwrapped geocoded interferogram products. We spatially average the full resolution wrapped interferograms by a factor of 19 in the range direction and 7 in the azimuth direction, resulting in pixels that are approximately 90 m in scale. For the “masked” version of the dataset, only the unmasked pixels are used in this spatial averaging. In places where there are no unmasked pixels within the 19x7 spatial averaging window, the spatially averaged, masked interferogram is undefined. For the unmasked interferograms, we apply a Goldstein-Werner filter with $\alpha = 0.1$ (Goldstein and Werner, 1998), then unwrap the interferograms using SNAPHU (Chen and Zebker, 2002), resulting in the filtered, unwrapped version of the unmasked phase, φ_{unw}^{umask} .

Filtering and unwrapping the masked interferograms is more challenging because of the undefined/masked values present within each interferogram. We address this by assuming that, within the set of stable pixels, the difference between the unwrapped phase values and the unwrapped, filtered phase values in the unmasked dataset, φ_{unw}^{umask} , falls within the range $[-\pi, \pi]$. Where this assumption holds, the 2π phase ambiguity needed to define the unwrapped, masked interferometric phase, φ_{unw}^{mask} , can be solved for (e.g., Tymofeyeva et al., 2019; Jiang and Lohman, 2021):

$$\varphi_{unw}^{mask} = \text{arg}(\Delta\varphi_{i,i+1}) + \varphi_{unw}^{umask} \quad (6)$$

where $\Delta\varphi_{i,i+1}$ is the difference in phase between the spatially averaged, filtered, unmasked interferogram between dates i and $i+1$, and the spatially averaged, masked interferogram.

We produce displacement time series and inferred average displacement rates using the standard workflow from open source Miami INsar Time-series software in PYthon (MintPy) (Zhang et al., 2019). We use the same reference pixel for each inversion and use the sign

convention such that subsidence is associated with a negative velocity in the LOS direction. We apply this approach to both the sets of interferograms and compare the results in Section 4.

3.3.2 Synthetic time series, based on observed field biases

We use the phase bias φ_{bias} described above for each field and for each interferogram to construct synthetic time series (Figure 3). We begin by constructing synthetic full resolution wrapped interferograms containing only the signal observed from each field for that time period. We assign the observed phase bias recorded in Section 3.2 for that given interferogram. If this criterion is not met, then the assigned bias is zero. We introduce Gaussian noise scaled to be consistent with the coherence γ of the actual interferogram:

$$\sigma = \sqrt{-2 \ln(\gamma)} \quad (7)$$

where σ is the standard deviation and γ is the absolute value of the complex coherence in Eq. 4. After generating these full-resolution synthetic interferograms, we process them and infer velocity using the same workflow as we used for the real data (described above).

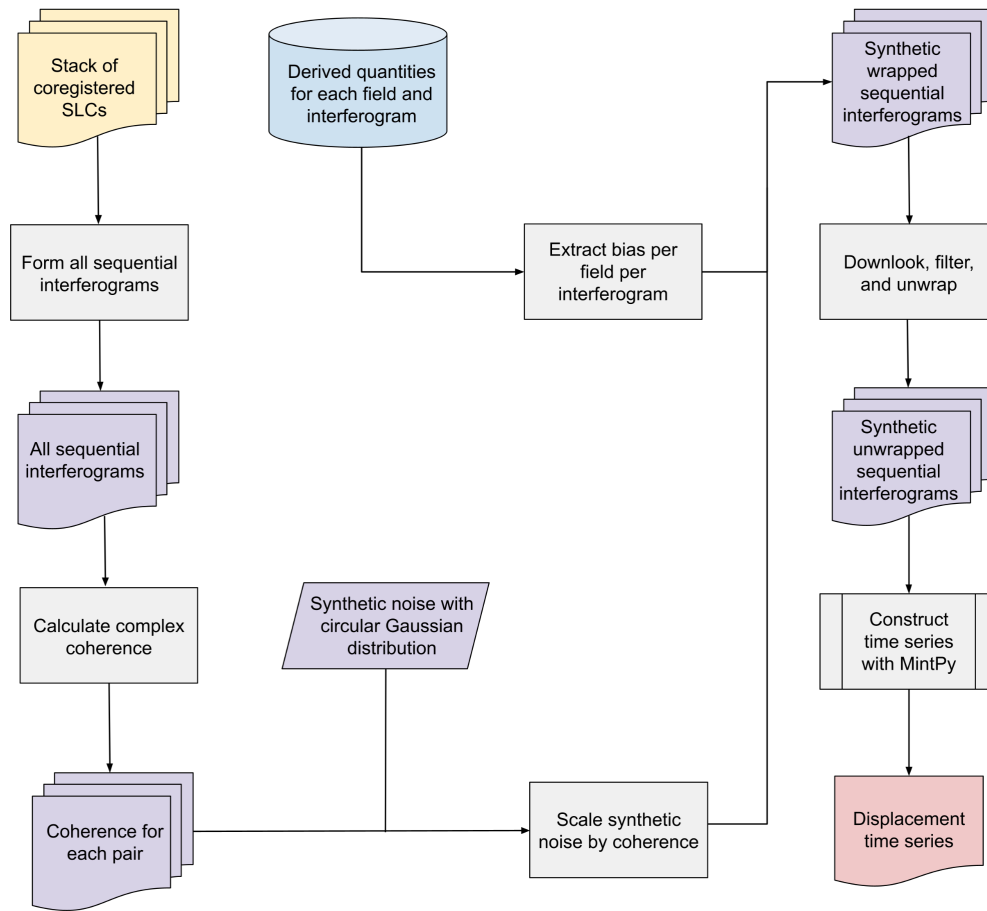


Figure 3: Workflow for synthetic time series. Initial and end result datasets represented by bolded outline. Colors indicate coregistered SLCs (yellow), complex-valued datasets from InSAR (purple), CDL and CDL-derived products (green), average phase bias calculated in Figure 2 (blue), and final synthetic displacement time series (red). Gray rectangles represent processes to manipulation of datasets, and white diamond represents determination of whether each field is sufficiently coherent. Details of MintPy are described in (Zhang et al., 2019).

4. Results

4.1 Relationship between phase bias and crop type

Our analysis includes 3167 individual fields that are flagged in the CDL database as one of the six crops we focus on (almonds, cotton, grapes, pistachios, tomatoes, and winter wheat). Figure 4 shows an example of the sharp phase transitions at field boundaries that are present through this dataset.

Figure 5 shows phase bias over time for each crop type. In each panel, the phase bias is shown for each field of that crop type, for each interferogram, except for when <10% of the pixels in that field or in the surrounding “stable” pixels had coherence > 0.3. Cotton is associated with the largest average phase bias and a strong seasonality. Cotton and tomato fields are heavily decorrelated between July and September. Almonds and pistachios also are associated with a clear seasonal phase bias, without the annual loss of coherence observed within the cotton fields. Grapes, tomatoes, and winter wheat have small to negligible phase bias. The other four crops are coherent for the majority of our time frame.

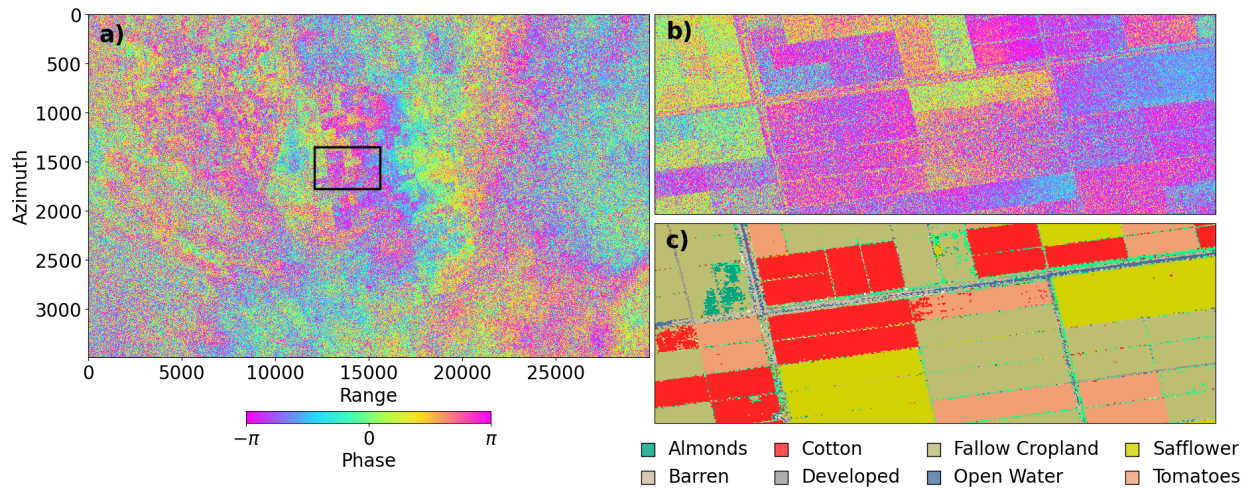


Figure 4: (a) Six day full resolution wrapped interferogram between 2021-01-23 and 2021-01-29 of the entire study region in radar coordinates. Black box outlines zoomed in subregion of (b); (b) Subregion of (a) showing sharp contrast between fields and adjacent roads. Interferogram is wrapped on $[-\pi, \pi]$ interval; (c) CDL in radar coordinates in with the eight most common land cover types of subregion (b).

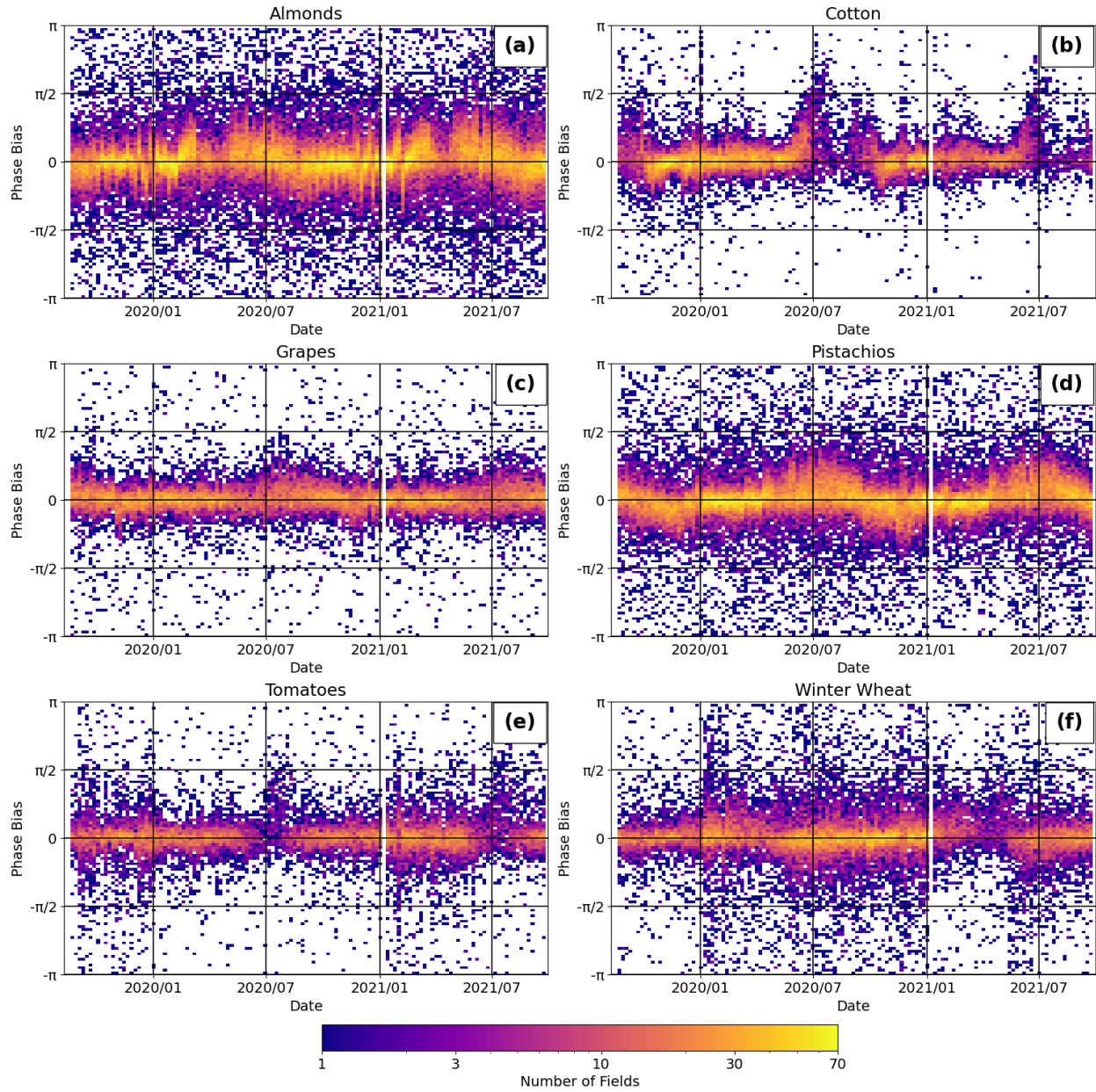


Figure 5: Heatmap of phase bias over time for each crop type. Each heatmap only includes biases at times when at least 10% of possible field and road pixels have coherence > 0.3 .

4.2 NDVI and phase bias

In this section we compare the temporal behavior of NDVI averaged over each field with the average phase bias. Here we show the comparison against cotton, but other crop type comparisons can be found in the supplemental material. NDVI is a completely independent observation type and helps to illustrate the correspondence between the temporal variations in phase bias and phenological stage, particularly for cotton (Figure 6a,b). Rising NDVI values near the end of each year coincide with an increase in phase bias, followed by a time period of

decorrelation when NDVI values are at a maximum. This indicates that the large phase biases we observe in cotton are associated with a time period where the cotton plants are beginning to grow, but the fields become decorrelated during the time period of peak vegetation density, as indicated by the peak in NDVI.

Tomatoes and winter wheat also have strong seasonal NDVI cycles, but their phase biases do not show similar temporal behavior (Figures S6, S7). The NDVI of almonds (Figure S3), grapes (Figure S4), and pistachios (Figure S5) behave similarly over time. Some fields follow a seasonal cycle between high and low NDVI, but there are many fields that have low NDVI during the entirety of our study period. Note that all figures showing NDVI over time include all fields containing the specific crop. Some of these fields are too decorrelated to include in our phase bias analysis.

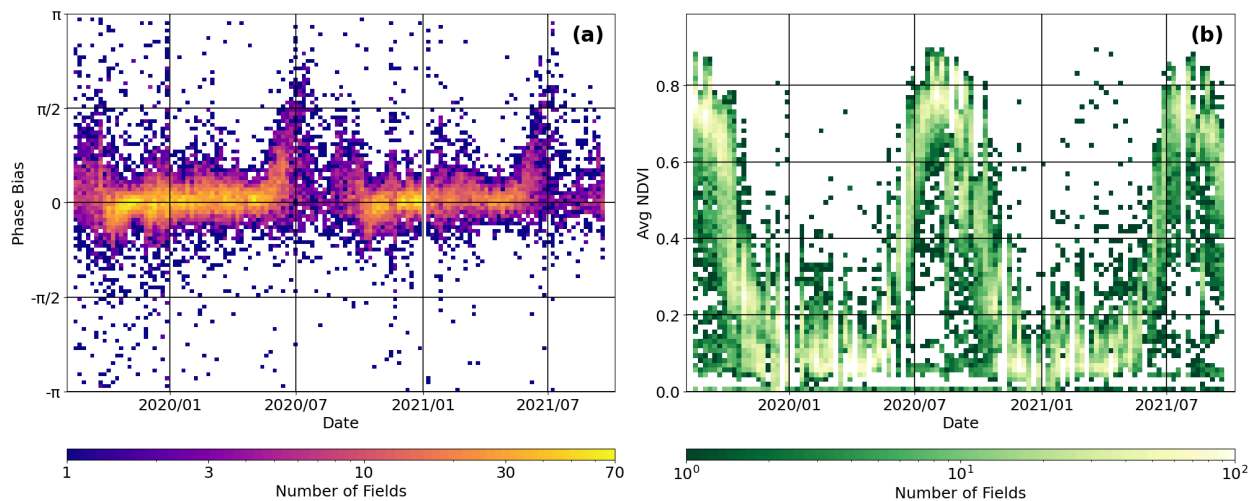


Figure 6: a) Phase bias heatmap of cotton fields over time; b) NDVI heatmap of cotton fields over time.

4.3 Time series inversion results

4.3.1 Real-data time series results

As described above, many current workflows for generating InSAR time series products (e.g., Bekaert et al., 2019) include some component of spatial filtering in their analysis. In areas with heterogeneous land cover, this filtering may combine pixels from areas with different characteristics in ways that are undesirable. We generate two time series: one using the standard approach (all possible pixels), and one where we mask out all but the “stable” pixels at full resolution before any further spatial averaging or filtering.

Figure 7 shows the inferred average LOS velocity for both approaches. Peak subsidence is around -30 cm/yr using either method (Figure 7a,b). Figure 7c shows the difference between the two inversions, and Figure 7d spatially filtered for better visualization. Figure 8a focuses on a

subregion of the study site, along a road with large fields (cotton for most of the study time interval) to the north and south (Figure 8b). Note the pronounced difference of ~ 2 cm/yr between the unfiltered/masked and the filtered/unmasked inversions. This difference is due to phase biases in the adjacent fields impacting the inferred phase values along the roads after spatial averaging and filtering.

4.3.2 Synthetic time series results

The synthetic time series inversion (described in Section 3.3) demonstrates the effect of our observed phase bias over time within each field. We use the same reference pixel as in Section 4.3.1. The inferred LOS velocity varies between individual fields (Figure 9a), with large (cm/yr or more) negative values within the central portion of our study area. Most fields have biases between -2.5 (subsidence) and 1 (uplift) cm/yr (Figure 9b). The largest magnitude biases occur within the artificially drained Tulare Lake, where the majority of cotton fields are located. This is consistent with our observations of cotton having the most distinct phase biases over time. Note that the features visible in Figure 9a are solely due to the observed biases in each individual field. This is in contrast to the rate differences shown in Figure 7c,d, which are attributable to spatial filtering over heterogeneous land covers (agricultural fields together with stable pixels).

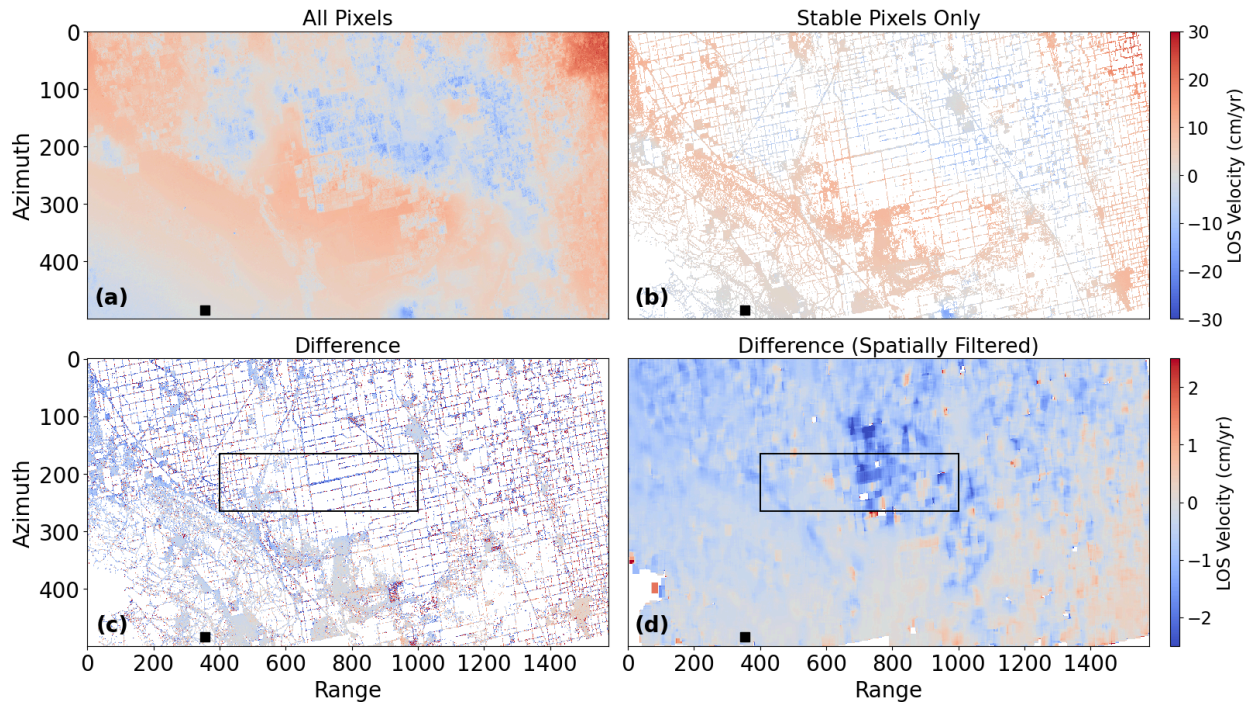


Figure 7: a) Time series inversion using all pixels; b) Time series inversion using only stable pixels; c) Difference between two time series. Black box denotes subregion shown in Figure 8a; d) Difference spatially filtered by a factor of 20×20 for visualization purposes. Reference point shown as a black square.

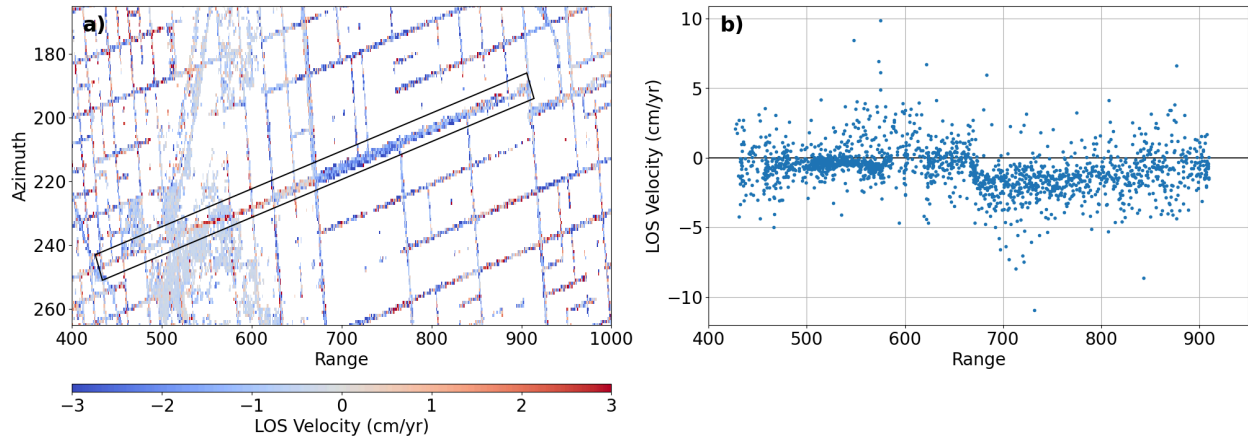


Figure 8: a) Zoomed-in area from Figure 7c of difference between inverting with all pixels and using stable pixels only. Black box outlines pixels shown in (b); b) Profile of pixels within black box in (a).

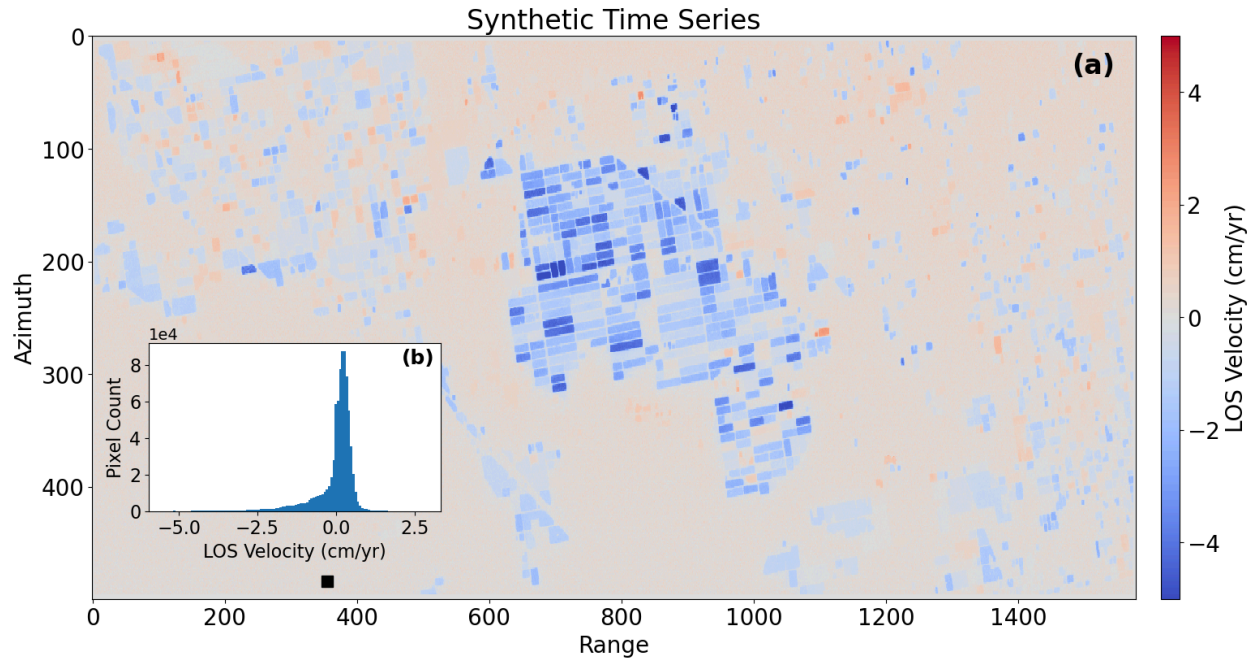


Figure 9: a) LOS velocity inversion of synthetic interferograms. Positive values indicate movement toward the satellite (uplift), and negative values indicate movement away from the satellite (subsidence). Reference point shown as a black square; b) Histogram of LOS velocities.

5. Discussion and Conclusion

In agricultural regions where groundwater resources are being heavily utilized, InSAR-derived rates can help with characterizing and managing such resources (e.g., Amelung et al., 1999; Chaussard et al., 2014; Farr, 2016; Gao et al., 2018; Hussain et al., 2022; Kang and Knight, 2023; Motagh et al., 2017; Murray and Lohman, 2018; Neely et al., 2020). However,

contributions to the InSAR observations from other factors, such as soil moisture or vegetation characteristics, could bias such observations. In this paper, we examine an approach for mitigating this effect, as well as a method for characterizing how strong the effect could be. The largest biases we observe occur within cotton fields, although we also observe significant biases and seasonal signals in almond and pistachio orchards. In general, phase bias and NDVI are correlated with each other, suggesting that the bias is due to vegetation effects on the InSAR signal. However, factors like soil moisture may also be correlated with NDVI and may also contribute to the observed biases. Future work that includes the collection of in situ soil moisture measurements may help with efforts to separate out vegetation water content from soil moisture effects.

It is likely that some pixels are mislabeled in the CDL database, particularly since the database is only published once a year and may, therefore, miss time periods where a given field is switched from one crop to another. Because we invert for LOS velocity on a field-by-field basis, independent of land cover type, this potential CDL-based issue will not impact our inferred displacement rates over the region (Figures 7-9). However, mislabeling of individual fields will affect our summaries of individual crop types (Figures 5-6), and is only mitigated by the large number of fields that go into each summary.

In general, we observe a bias of ~2-4 cm/year of subsidence, both through our comparison of masked vs. unmasked interferograms (Figure 7) and through our modeling of the effect on each individual field over time (Figure 9). The small size of our study region results in some artifacts when compared to previous studies using the same data (e.g., Farr, 2016; Kang and Knight, 2023; Murray and Lohman, 2018; Neely et al., 2020). We attribute the uplift signal we see in the northeast corner of Figure 7a,b to the proximity of the reference point to the subsidence bowl. However, these considerations would not impact either the difference between the masked vs. unmasked time series, or the field-based results. We show that removing pixels that may exhibit suspect behavior, at the highest resolution possible, can help mitigate these biases at low computational cost, without requiring that the user produce more computationally expensive full-resolution displacement maps or perform persistent scatterer analyses (e.g., Ferretti et al., 2000; Hooper et al., 2004).

The peak subsidence rate within the San Joaquin Valley is ~30 cm/yr (e.g., Farr, 2016; Kang and Knight, 2023; Murray and Lohman, 2018; Neely et al., 2020), which is an order of magnitude larger than our observed bias. However, while the biases may be insignificant when compared to the signals in this particular region, researchers studying regions with smaller deformation signals or who are interested in analyzing shorter-term variations or seasonality in the subsidence in California, may find it useful to adopt some of the approaches described here.

Acknowledgements

This work was supported by NASA grants: 80NSSC19K1496, 80NSSC23K0721, and 80NSSC22K0460. Copernicus Sentinel-1 data 2019–2021 was retrieved from ASF DAAC 1 October 2021, processed by ESA, <https://www.asf.alaska.edu>.

Open Research Statement

All raw data used in this analysis are free and open, as is all the software used to prepare analysis-ready data. ESA Sentinel-1a/b data are available through ASF DAAC (<https://search.asf.alaska.edu/>) with a free Earthdata account (<https://www.earthdata.nasa.gov/>). CDL data are openly available via the CroplandCROS website (<https://croplandcros.scinet.usda.gov/>). Landsat 8 and Sentinel-2 imagery are accessed through Google Earth Engine (<https://earthengine.google.com/>). ISCE2 software and the Sentinel stack processor are available on Github (<https://github.com/isce-framework/isce2>). STRM DEM obtained using the software package sardem on Github (<https://github.com/scottstanie/sardem>). MintPy software is available on Github (<https://github.com/insarlab/MintPy>). Additional code developed by the authors for this project is available on Github (<https://github.com/kdevlin525/C-band-phase-bias>).

References

- Amelung, F., Galloway, D.L., Bell, J.W., Zebker, H.A., Laczniak, R.J., 1999. Sensing the ups and downs of Las Vegas: InSAR reveals structural control of land subsidence and aquifer-system deformation. *Geology* 27, 483–486. [https://doi.org/10.1130/0091-7613\(1999\)027<0483:STUADO>2.3.CO;2](https://doi.org/10.1130/0091-7613(1999)027<0483:STUADO>2.3.CO;2)
- Asner, G.P., Brodrick, P.G., Anderson, C.B., Vaughn, N., Knapp, D.E., Martin, R.E., 2016. Progressive forest canopy water loss during the 2012–2015 California drought. *Proc. Natl. Acad. Sci.* 113, E249–E255. <https://doi.org/10.1073/pnas.1523397113>
- Bekaert, D.P., Karim, M., Linick, J.P., Hua, H., Sangha, S., Lucas, M., Malarout, N., Agram, P.S., Pan, L., Owen, S.E., Lai-Norling, J., 2019. Development of open-access Standardized InSAR Displacement Products by the Advanced Rapid Imaging and Analysis (ARIA) Project for Natural Hazards. AGU Fall Meet. Abstr. 2019, G23A-04.
- Butler, J.J., Bohling, G.C., Whittemore, D.O., Wilson, B.B., 2020. A roadblock on the path to aquifer sustainability: underestimating the impact of pumping reductions. *Environ. Res. Lett.* 15, 014003. <https://doi.org/10.1088/1748-9326/ab6002>
- Chaussard, E., Wdowinski, S., Cabral-Cano, E., Amelung, F., 2014. Land subsidence in central Mexico detected by ALOS InSAR time-series. *Remote Sens. Environ.* 140, 94–106. <https://doi.org/10.1016/j.rse.2013.08.038>
- Chen, C.W., Zebker, H.A., 2002. Phase unwrapping for large SAR interferograms: statistical segmentation and generalized network models. *IEEE Trans. Geosci. Remote Sens.* 40, 1709–1719. <https://doi.org/10.1109/TGRS.2002.802453>
- Copernicus Sentinel-2 (processed by ESA), 2021. MSI Level-2A BOA Reflectance Product. Collection 1. https://doi.org/10.5270/S2_-zmk9xsj
- Dall, J., 2007. InSAR Elevation Bias Caused by Penetration Into Uniform Volumes. *IEEE Trans. Geosci. Remote Sens.* 45, 2319–2324. <https://doi.org/10.1109/TGRS.2007.896613>
- De Zan, F., Gomba, G., 2018. Vegetation and soil moisture inversion from SAR closure phases: First experiments and results. *Remote Sens. Environ.* 217, 562–572. <https://doi.org/10.1016/j.rse.2018.08.034>
- Escriva-Bou, A., Hanak, E., Cole, S., Medellín-Azuara, J., 2023. The Future of Agriculture in the

- San Joaquin Valley. Public Policy Institute of California.
- Escriva-Bou, A., Hui, R., Maples, S., Medellín-Azuara, J., Harter, T., Lund, J.R., 2020. Planning for groundwater sustainability accounting for uncertainty and costs: An application to California's Central Valley. *J. Environ. Manage.* 264, 110426. <https://doi.org/10.1016/j.jenvman.2020.110426>
- Farr, T.G., 2016. InSAR measurements of subsidence in the Central Valley, California from 2007 - present, in: *Proceedings of EUSAR 2016: 11th European Conference on Synthetic Aperture Radar*. Presented at the Proceedings of EUSAR 2016: 11th European Conference on Synthetic Aperture Radar, pp. 1–3.
- Farr, T.G., Rosen, P.A., Caro, E., Crippen, R., Duren, R., Hensley, S., Kobrick, M., Paller, M., Rodriguez, E., Roth, L., Seal, D., Shaffer, S., Shimada, J., Umland, J., Werner, M., Oskin, M., Burbank, D., Alsdorf, D., 2007. The Shuttle Radar Topography Mission. *Rev. Geophys.* 45. <https://doi.org/10.1029/2005RG000183>
- Fattahi, H., Agram, P., Simons, M., 2017. A Network-Based Enhanced Spectral Diversity Approach for TOPS Time-Series Analysis. *IEEE Trans. Geosci. Remote Sens.* 55, 777–786. <https://doi.org/10.1109/TGRS.2016.2614925>
- Ferretti, A., Prati, C., Rocca, F., 2000. Nonlinear subsidence rate estimation using permanent scatterers in differential SAR interferometry. *IEEE Trans. Geosci. Remote Sens.* 38, 2202–2212. <https://doi.org/10.1109/36.868878>
- Gabriel, A.K., Goldstein, R.M., Zebker, H.A., 1989. Mapping small elevation changes over large areas: Differential radar interferometry. *J. Geophys. Res. Solid Earth* 94, 9183–9191. <https://doi.org/10.1029/JB094iB07p09183>
- Gao, M., Gong, H., Chen, B., Li, X., Zhou, C., Shi, M., Si, Y., Chen, Z., Duan, G., 2018. Regional Land Subsidence Analysis in Eastern Beijing Plain by InSAR Time Series and Wavelet Transforms. *Remote Sens.* 10, 365. <https://doi.org/10.3390/rs10030365>
- Gleeson, T., Wada, Y., Bierkens, M.F.P., van Beek, L.P.H., 2012. Water balance of global aquifers revealed by groundwater footprint. *Nature* 488, 197–200. <https://doi.org/10.1038/nature11295>
- Goldstein, R.M., Werner, C.L., 1998. Radar interferogram filtering for geophysical applications. *Geophys. Res. Lett.* 25, 4035–4038. <https://doi.org/10.1029/1998GL900033>
- Gorelick, N., Hancher, M., Dixon, M., Ilyushchenko, S., Thau, D., Moore, R., 2017. Google Earth Engine: Planetary-scale geospatial analysis for everyone. *Remote Sens. Environ., Big Remotely Sensed Data: tools, applications and experiences* 202, 18–27. <https://doi.org/10.1016/j.rse.2017.06.031>
- Hasan, M.F., Smith, R., Vajedian, S., Pommerenke, R., Majumdar, S., 2023. Global land subsidence mapping reveals widespread loss of aquifer storage capacity. *Nat. Commun.* 14, 6180. <https://doi.org/10.1038/s41467-023-41933-z>
- Hooper, A., Zebker, H., Segall, P., Kampes, B., 2004. A new method for measuring deformation on volcanoes and other natural terrains using InSAR persistent scatterers. *Geophys. Res. Lett.* 31. <https://doi.org/10.1029/2004GL021737>
- Hussain, M.A., Chen, Z., Zheng, Y., Shoaib, M., Ma, J., Ahmad, I., Asghar, A., Khan, J., 2022. PS-InSAR Based Monitoring of Land Subsidence by Groundwater Extraction for Lahore Metropolitan City, Pakistan. *Remote Sens.* 14, 3950. <https://doi.org/10.3390/rs14163950>
- Jiang, J., Lohman, R.B., 2021. Coherence-guided InSAR deformation analysis in the presence of ongoing land surface changes in the Imperial Valley, California. *Remote Sens. Environ.* 253, 112160. <https://doi.org/10.1016/j.rse.2020.112160>
- Kang, S., Knight, R., 2023. Isolating the Poroelastic Response of the Groundwater System in InSAR Data From the Central Valley of California. *Geophys. Res. Lett.* 50, e2023GL103222. <https://doi.org/10.1029/2023GL103222>
- Mall, N.K., Herman, J.D., 2019. Water shortage risks from perennial crop expansion in California's Central Valley. *Environ. Res. Lett.* 14, 104014.

- <https://doi.org/10.1088/1748-9326/ab4035>
- Massonnet, D., Rossi, M., Carmona, C., Adragna, F., Peltzer, G., Feigl, K., Rabaute, T., 1993. The displacement field of the Landers earthquake mapped by radar interferometry. *Nature* 364, 138–142. <https://doi.org/10.1038/364138a0>
- Motagh, M., Shamshiri, R., Haghshenas Haghighi, M., Wetzel, H.-U., Akbari, B., Nahavandchi, H., Roessner, S., Arabi, S., 2017. Quantifying groundwater exploitation induced subsidence in the Rafsanjan plain, southeastern Iran, using InSAR time-series and in situ measurements. *Eng. Geol.* 218, 134–151. <https://doi.org/10.1016/j.enggeo.2017.01.011>
- Murray, K.D., Lohman, R.B., 2018. Short-lived pause in Central California subsidence after heavy winter precipitation of 2017. *Sci. Adv.* 4, eaar8144.
- Neely, W.R., Borsa, A.A., Silverii, F., 2020. GInSAR: A cGPS Correction for Enhanced InSAR Time Series. *IEEE Trans. Geosci. Remote Sens.* 58, 136–146. <https://doi.org/10.1109/TGRS.2019.2934118>
- Nishikawa, T., Siade, A., Reichard, E., Ponti, D., Canales, A., Johnson, T., 2009. Stratigraphic controls on seawater intrusion and implications for groundwater management, Dominguez Gap area of Los Angeles, California, USA. *Hydrogeol. J.* 17, 1699–1725. <https://doi.org/10.1007/s10040-009-0481-8>
- Petersen-Perlman, J.D., Aguilar-Barajas, I., Megdal, S.B., 2022. Drought and groundwater management: Interconnections, challenges, and policy responses. *Curr. Opin. Environ. Sci. Health* 28, 100364. <https://doi.org/10.1016/j.coesh.2022.100364>
- Poland, J.F., Lofgren, B.E., Ireland, R.L., Pugh, R.G., 1975. Land Subsidence in the San Joaquin Valley, California, As of 1972. *Geol. Surv. Prof. Pap.* 437-H.
- Richey, A.S., Thomas, B.F., Lo, M.-H., Reager, J.T., Famiglietti, J.S., Voss, K., Swenson, S., Rodell, M., 2015. Quantifying renewable groundwater stress with GRACE. *Water Resour. Res.* 51, 5217–5238. <https://doi.org/10.1002/2015WR017349>
- Rohde, M.M., Albano, C.M., Huggins, X., Klausmeyer, K.R., Morton, C., Sharman, A., Zaveri, E., Saito, L., Freed, Z., Howard, J.K., Job, N., Richter, H., Toderich, K., Rodella, A.-S., Gleeson, T., Huntington, J., Chandanpurkar, H.A., Purdy, A.J., Famiglietti, J.S., Singer, M.B., Roberts, D.A., Caylor, K., Stella, J.C., 2024. Groundwater-dependent ecosystem map exposes global dryland protection needs. *Nature* 632, 101–107. <https://doi.org/10.1038/s41586-024-07702-8>
- Rosen, P.A., Gurrola, E., Sacco, G.F., Zebker, H., 2012. The InSAR scientific computing environment, in: *EUSAR 2012; 9th European Conference on Synthetic Aperture Radar*. Presented at the EUSAR 2012; 9th European Conference on Synthetic Aperture Radar, pp. 730–733.
- Tymofyeyeva, E., Fialko, Y., Jiang, J., Xu, X., Sandwell, D., Bilham, R., Rockwell, T.K., Blanton, C., Burkett, F., Gontz, A., Moafipoor, S., 2019. Slow Slip Event On the Southern San Andreas Fault Triggered by the 2017 M8.2 Chiapas (Mexico) Earthquake. *J. Geophys. Res. Solid Earth* 124, 9956–9975. <https://doi.org/10.1029/2018JB016765>
- USDA NASS, 2021. Cropland Data Layer: United States Department of Agriculture (USDA) National Agricultural Statistics Service (NASS) [WWW Document]. USDA NASS Mark. Inf. Serv. Off. Wash. DC. URL <https://croplandcros.scinet.usda.gov/> (accessed 10.1.21).
- Wada, Y., van Beek, L.P.H., van Kempen, C.M., Reckman, J.W.T.M., Vasak, S., Bierkens, M.F.P., 2010. Global depletion of groundwater resources. *Geophys. Res. Lett.* 37. <https://doi.org/10.1029/2010GL044571>
- Zebker, H.A., Villasenor, J., 1992. Decorrelation in interferometric radar echoes. *IEEE Trans. Geosci. Remote Sens.* 30, 950–959. <https://doi.org/10.1109/36.175330>
- Zhang, Y., Fattahi, H., Amelung, F., 2019. Small baseline InSAR time series analysis: Unwrapping error correction and noise reduction. *Comput. Geosci.* 133, 104331. <https://doi.org/10.1016/j.cageo.2019.104331>

- Zheng, Y., Fattahi, H., Agram, P., Simons, M., Rosen, P., 2022. On Closure Phase and Systematic Bias in Multilooked SAR Interferometry. *IEEE Trans. Geosci. Remote Sens.* 60, 1–11. <https://doi.org/10.1109/TGRS.2022.3167648>
- Zwieback, S., Hensley, S., Hajnsek, I., 2015. Assessment of soil moisture effects on L-band radar interferometry. *Remote Sens. Environ.* 164, 77–89. <https://doi.org/10.1016/j.rse.2015.04.012>

Supplemental

Introduction

This section contains Supplemental Information for the paper, “Evaluation of Vegetation Bias in InSAR Time Series for Agricultural Areas within the San Joaquin Valley, CA”. Figure S1 provides information on pixels used in our analysis. Figures S2-S7 provide additional information on the relationship between phase bias and NDVI for cotton, almonds, grapes, pistachios, tomatoes, and winter wheat.

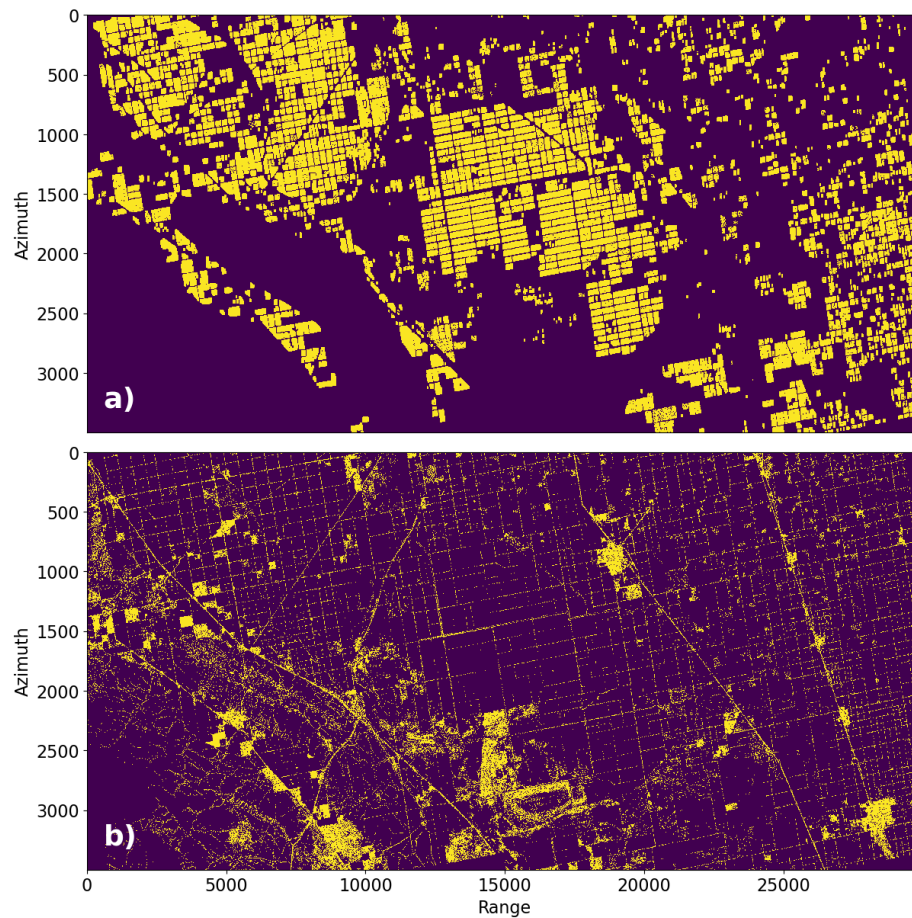


Figure S1: a) All pixels included in fields used in analysis shown in yellow; b) All pixels included in roads and stable regions shown in yellow.

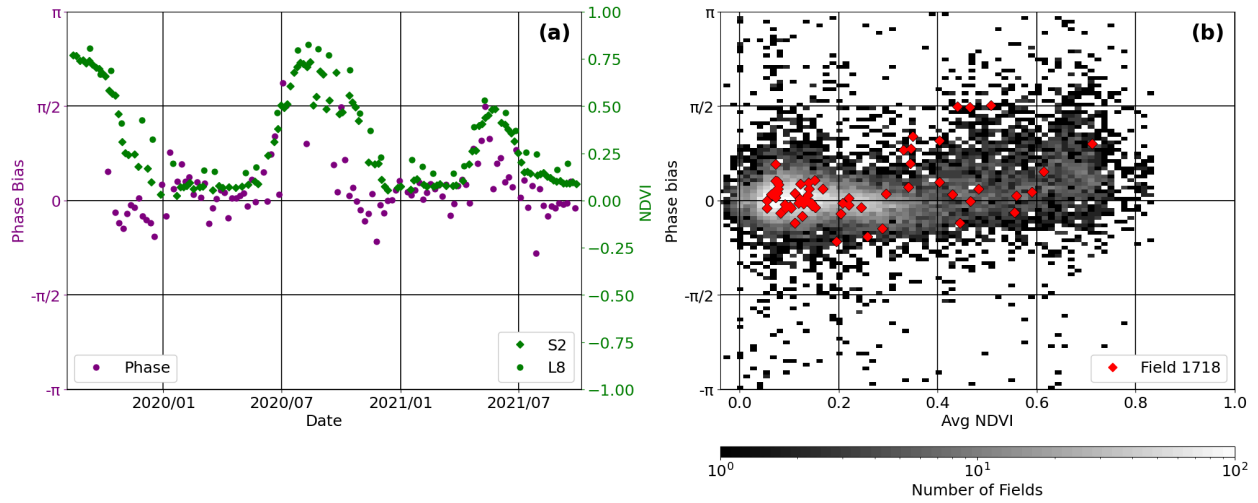


Figure S2: a) Phase bias and NDVI over time for example cotton field (Field 1718); b) Heatmap of interpolated NDVI vs. phase bias for cotton fields, with values for Field 1718 shown as red diamonds.

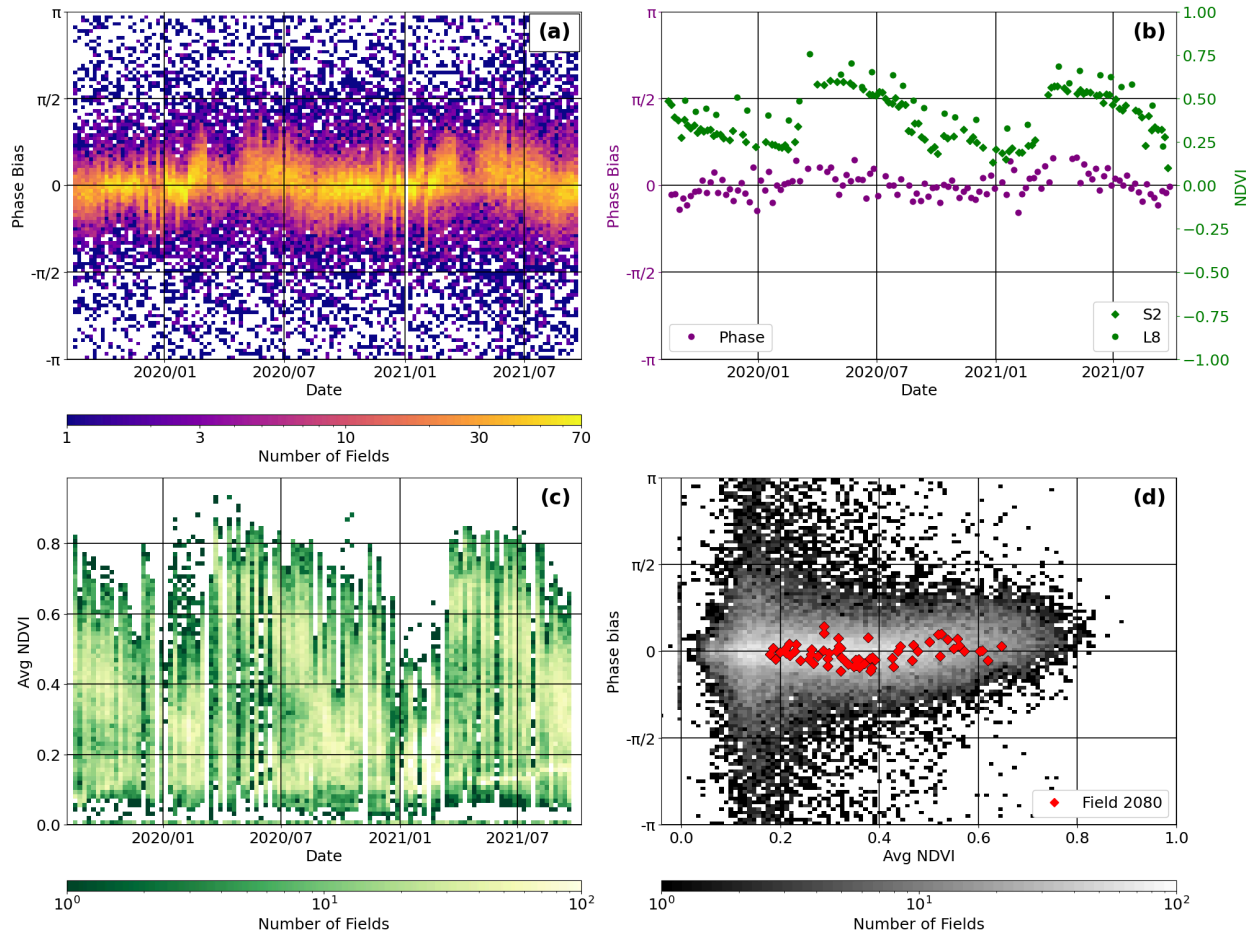


Figure S3: a) Phase bias heatmap of almond fields over time; b) Phase bias and NDVI over time for example almond field (Filed 2080); c) NDVI heatmap of almond fields over time; d) Heatmap of interpolated NDVI vs. phase bias for almond fields, with values for Field 2080 shown as red diamonds.

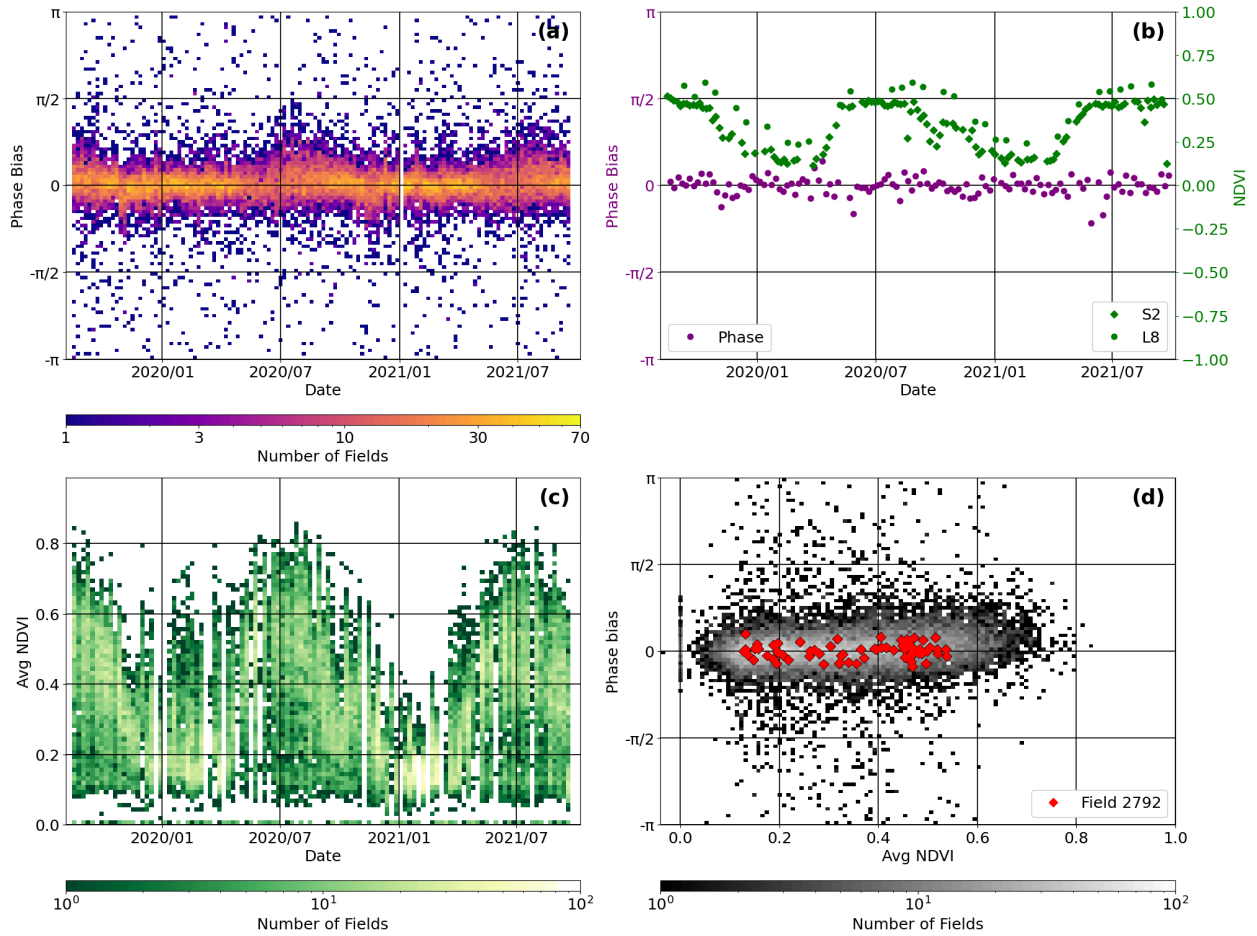


Figure S4: a) Phase bias heatmap of grape fields over time; b) Phase bias and NDVI over time for example grape field (Field 2792); c) NDVI heatmap of grape fields over time; d) Heatmap of interpolated NDVI vs. phase bias for grape fields, with values for Field 2792 shown as red diamonds.

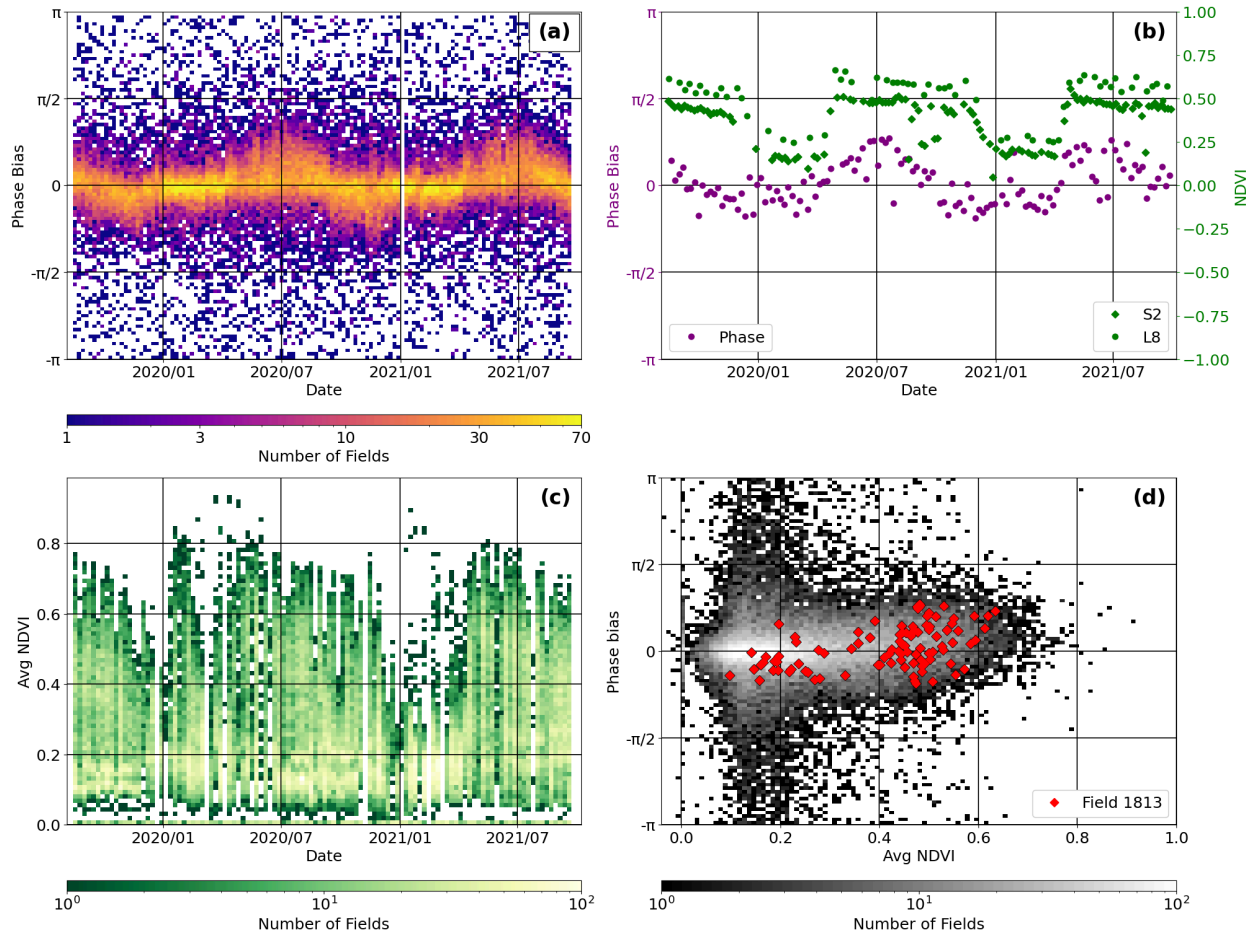


Figure S5: a) Phase bias heatmap of pistachio fields over time; b) Phase bias and NDVI over time for example pistachio field (Field 1813); c) NDVI heatmap of pistachio fields over time; d) Heatmap of interpolated NDVI vs. phase bias for pistachio fields, with values for Field 1813 shown as red diamonds.

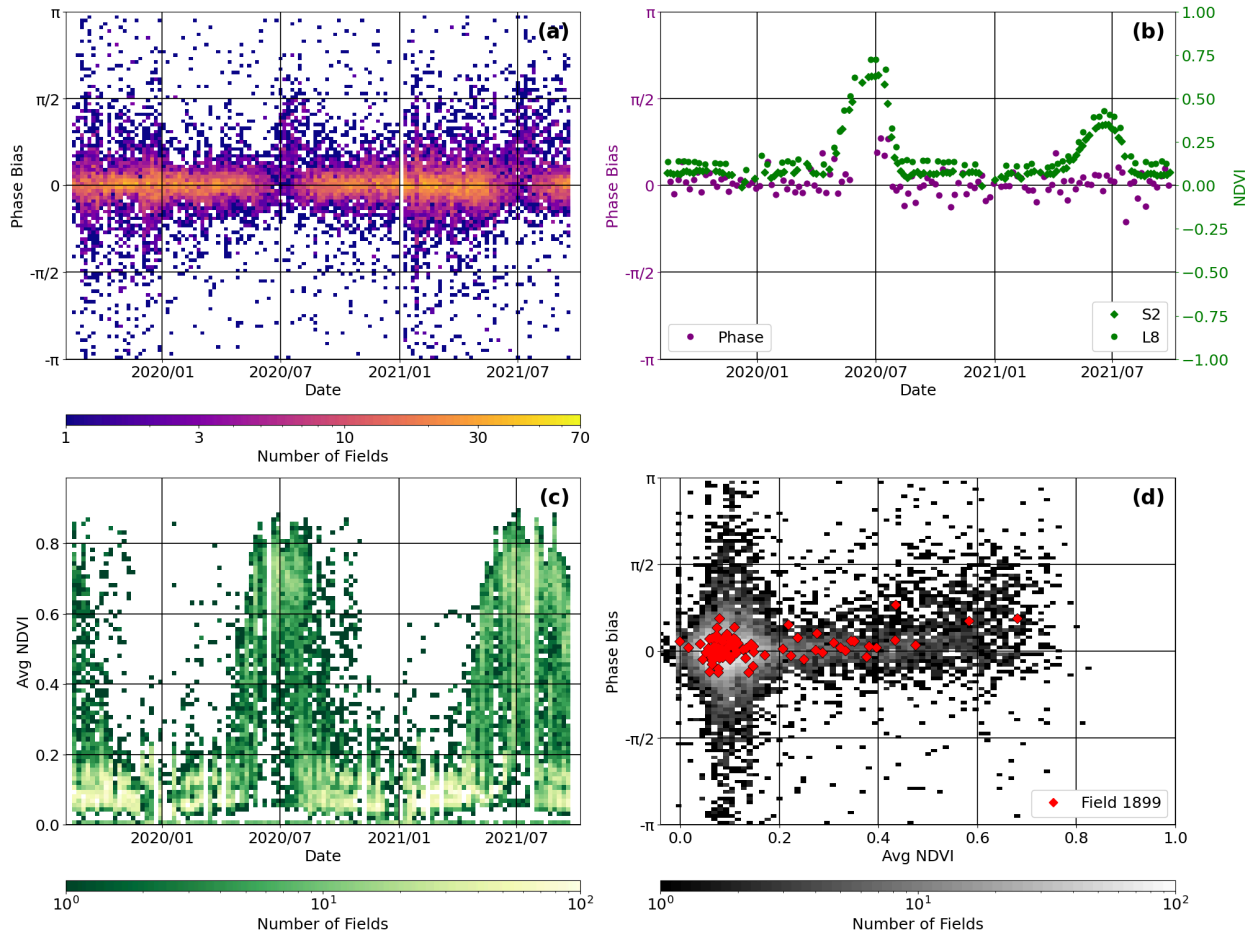


Figure S6: a) Phase bias heatmap of tomato fields over time; b) Phase bias and NDVI over time for example tomato field (Field 1899); c) NDVI heatmap of tomato fields over time; d) Heatmap of interpolated NDVI vs. phase bias for tomato fields, with values for Field 1899 shown as red diamonds.

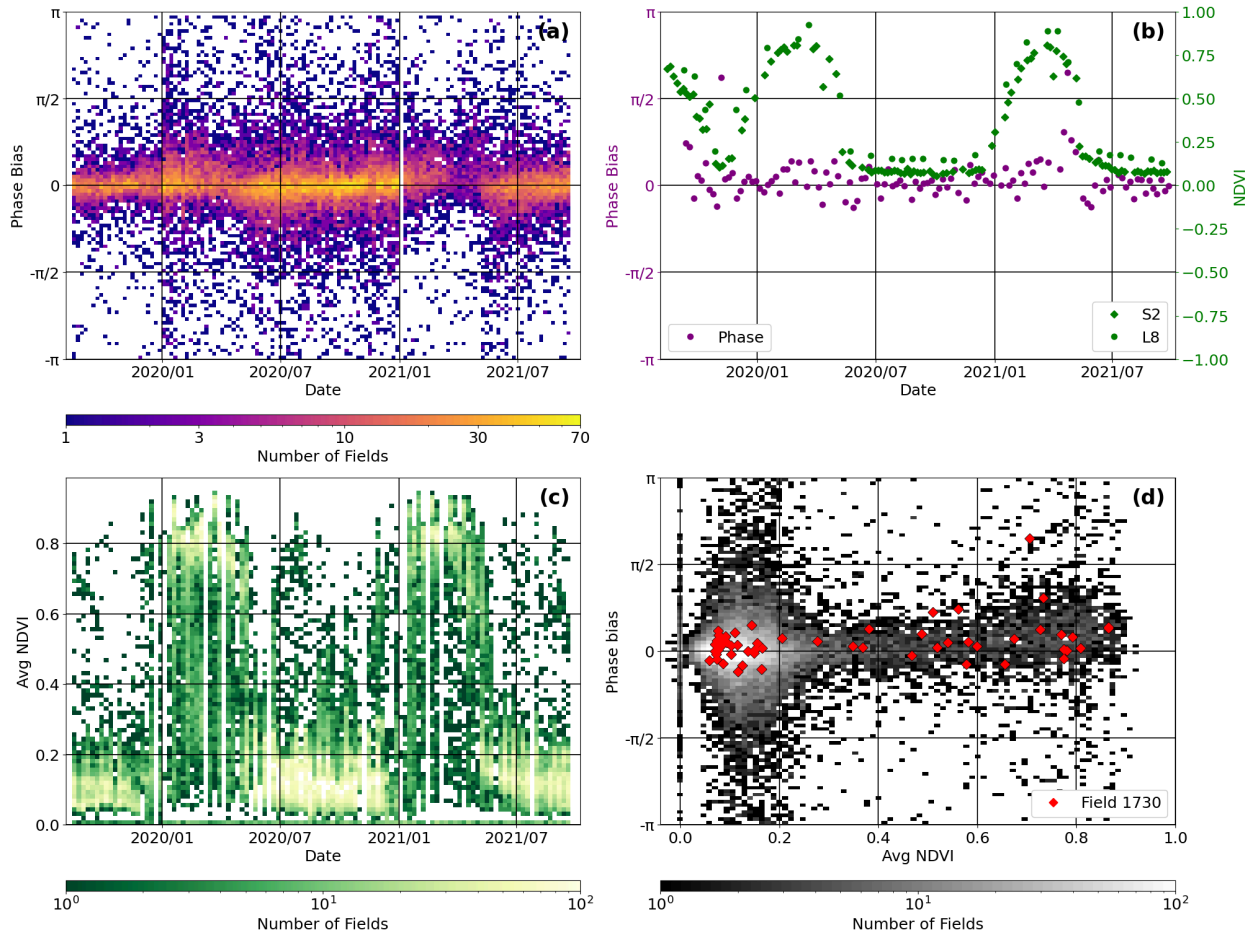


Figure S7: a) Phase bias heatmap of winter wheat fields over time; b) Phase bias and NDVI over time for example winter wheat field (Field 1730); c) NDVI heatmap of winter wheat fields over time; d) Heatmap of interpolated NDVI vs. phase bias for winter wheat fields, with values for Field 1730 shown as red diamonds.